SOLUTION MINING RESEARCH INSTITUTE
679 Plank Road
Clifton Park, NY 12065, USA

Telephone: +1 518-579-6587
www.solutionmining.org

Technical Conference Paper

1965 – 2025

Benchmarking Constitutive Models for Salt Cavern Design in Underground Hydrogen Storage

Dirk Zapf & Feline Körner
Leibniz University, IGtH-IUB, Hannover, Germany

Hippolyte Djizanne & Hajar Habbani
Ineris, Verneuil-en-Halatte, France

SMRI Fall 2025 Technical Conference
29-30 September 2025
Wichita, Kansas, United States

Solution Mining Research Institute Fall 2025 Technical Conference

Wichita, Kansas, United States 29-30 September 2025

BENCHMARKING CONSTITUTIVE MODELS FOR SALT CAVERN DESIGN IN UNDERGROUND HYDROGEN STORAGE

Dirk Zapf[(1)], Hippolyte Djizanne[(2)], Feline Körner[(1)] & Hajar Habbani[(2)]

[(1)] Leibniz University, IGtH-IUB, Hannover, Germany

[(2)] Ineris, Verneuil-en-Halatte, France

Abstract

The design of salt caverns for Underground Hydrogen Storage (UHS) requires reliable mechanical models that can capture the time-dependent, nonlinear behavior of rock salt under cyclic and thermodynamic loading. Although a variety of constitutive models are currently used across the industry, their applicability and comparative performance in the context of hydrogen storage remain an open question. This study presents the first phase of a collaborative benchmark involving multiple expert teams and modeling tools, each of which has already demonstrated robust performance in the rock mechanics design of salt caverns for underground natural gas storage (UGS). The initial objective is to present and compare the various design philosophies and modeling approaches used in industrial practice, identifying key parameters of interest when transitioning from methane to hydrogen storage – such as cycle frequency, pressure-temperature coupling, and hydrogen-specific constraints. The second part of the study focuses on a comparative numerical analysis using both finite elements (LOCAS) and finite difference (FLAC3D) simulations. A reference geometry and loading scenario representative of future UHS operations is defined. Each team implements its preferred constitutive model (e.g., Munson-Dawson, Lubby2 (or Lubby-CF including damage and healing), or creep-damage variants) and computes stress redistribution, creep convergence, subsidence, and the evolution of the damaged rock salt zone. The benchmark intended to foster a technical discussion on the sources of variation in model outputs, stemming from differences in model structure, parameter calibration, and numerical implementation. The results offer valuable insights into the current modeling landscape and contribute to building a common understanding of the safe and efficient deployment of UHS systems in salt formations.

Keywords: Rock mechanics, Thermodynamics, Gas operation, Constitutive models, Hydrogen

Introduction

In Germany and France, the rock mechanics design of salt caverns is the responsibility of geotechnical engineers. Dimensioning concepts and constitutive models have been developed and used by companies and universities in recent years in both countries (Lemaitre 1971; Heusermann et al., 1982; Menzel & Schreiner, 1983; Vouille et al., 1984; Uraï et al., 1987; Eickemeier et al., 2002; Brückner et al., 2005; Karimi-Jafari et al., 2007; Schulz et al., 2011; Djizanne, 2014; Zapf, 2014; Yildirim, 2018), which differ in detail but all pursue the same goal: the safe storage of energy sources in salt caverns. The dimensioning criteria in this paper primarily concern gas storage caverns (e.g., natural gas or hydrogen). Except in cases of cavern abandonment or repurposing, the design of oil caverns does not require detailed consideration of thermodynamic processes, as these have little influence on the storage and withdrawal of the fluid. In that case, the stresses on the salt are more or less purely mechanical in nature. The dimensioning concepts for storing gases in salt caverns have been continuously developed over time. Even in times when numerical calculations were not yet available to the same extent as they are today, calculations and analyses were already being carried out to determine the maximum possible operating pressures. This paper describes the theoretical approaches to rock mechanical design of gas storage caverns in Germany and France, and compares them with an example that assesses the stress states surrounding a salt cavern.

1. Constitutive models for rock salt

Over the past few decades, numerous material models have been developed worldwide to characterize the mechanical behavior of rock salt, utilizing a wide range of theoretical approaches and mathematical frameworks. In Germany in particular, substantial research efforts have focused on the development, refinement, and benchmarking of constitutive models. From 2004 to 2022, four major collaborative research projects brought together leading institutions in the field of salt mechanics, including the University of Hannover, the Technical University of Braunschweig, the Technical University of Clausthal, and the Institute for Geomechanics (IfG, headed by Andreas Hampel). Earlier phases also involved the Federal Institute for Geosciences and Natural Resources (BGR) and the Karlsruhe Institute of Technology (KIT). The most recent of these projects was WEIMOS (e.g., Hampel et al., 2022; Lüdeling et al., 2022; Wolters & Sun-Kurczinski, 2022). These efforts combined systematic laboratory test campaigns, numerical back-analyses, and simulations of underground scenarios to advance constitutive modeling.

The thermomechanical behavior of rock salt is inherently complex. Modern constitutive laws must capture both transient and steady-state creep, dilatancy, damage evolution, and failure – along with the interdependencies between these phenomena. Most advanced models explicitly define the steady-state creep rate. In the following sections, we focus on the steady-state creep behavior of undamaged rock salt.

Creep laws typically express the strain rate as a function of deviatoric stress and a set of material-specific parameters. These parameters must be calibrated using laboratory experiments, *in-situ* measurements (e.g., convergence data), or general physical considerations. Once a parameter set is defined, the model can predict specific creep rates under given conditions.

Due to its polycrystalline NaCl structure, rock salt exhibits ductile deformation under compressive stress. On both macro- and microscale levels, its thermomechanical behavior shows notable similarities to that of metals and alloys, including the underlying deformation mechanisms and resulting microstructures. Accordingly, many constitutive models for rock salt are derived from theoretical frameworks initially developed for metallic materials. The material models investigated in the WEIMOS project vary significantly in their theoretical underpinnings and conceptual design. However, they share common features: the temperature dependence of creep is generally described using Arrhenius-type expressions, each associated with distinct activation energies for different creep mechanisms. Elastic deformation is modeled in all cases using Hooke's law, but the elastic moduli are formulated as damage-dependent, thereby allowing for the degradation of elastic stiffness as damage accumulates.

Constitutive models commonly used in salt mechanics can be broadly categorized into three groups:

- Microphysics-based models, such as the Composite Dilatancy Model (CDM),
- Macroscopic, phenomenological models with structural adaptation, e.g., Günther/Salzer,

- Rheological, viscoelastic-plastic models, such as the Minkley model, Lubby2 (Lubby-CF), Lux/Wolters/Lerche, TUBSsalt, Munson-Dawson, and Reedlunn's model from Sandia, which combine different approaches.

The rheological models are built upon classical mechanical elements such as springs (Hookean), dashpots (Newtonian), and friction blocks (St. Venant) to represent various creep components. Transient and steady-state creep are modeled as separate elements, often using combinations such as Kelvin and Maxwell bodies (Figure 1). The viscosity in the Maxwell dashpot is typically stress-, temperature-, and sometimes damage-dependent, allowing the Newtonian viscous behavior to be generalized and aligned with observed nonlinear creep responses.

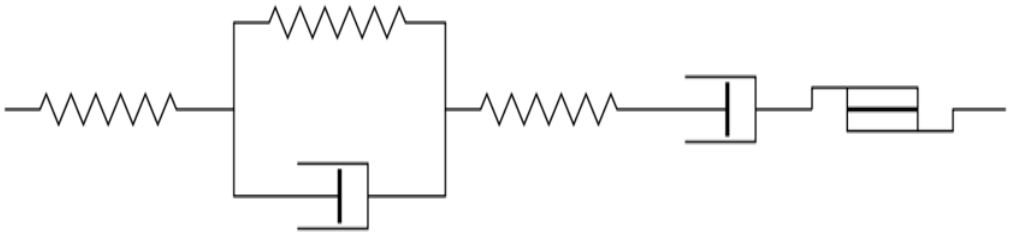

Figure 1. Schematic representation of the visco-elasto-plastic material model for salt rocks. Note that the "Hooke" and "Maxwell" springs correspond to volumetric (bulk) and deviatoric (shear) deformation.

Historically, constitutive models for steady-state creep were primarily derived from laboratory data exhibiting creep rates greater than 10^{-5}/day (≈10^{-10}/s). These rates correspond to differential stresses above 6–8 MPa at temperatures of up to 60 °C (140 °F). These are conditions associated with dislocation-dominated creep. Due to the lack of reliable experimental data at lower stress levels, such high-stress models (often using power laws with exponents n = 3 to 7) were extrapolated downward into the low-stress regime. Only a few tests had been carried out so far to determine the creep behavior under low deviatoric stress conditions.

However, simulations of real underground structures have demonstrated that these extrapolated models tend to underestimate deformations at low equivalent stress levels. Notably, the empirical Lubby creep law (Lux, 1983) introduced a stress-dependent exponential formulation to represent low-stress creep behavior better. This model, initially developed for engineering considerations in cavern design, has since provided realistic predictions under such conditions.

Although there are several material models for describing the mathematical-physical phenomena in rock salt, the material laws used in this paper are described in detail below.

1.1. Lubby2 / Lubby-CF

Lubby-CF (Yildirim et al., 2016; Yildirim & Zapf, 2022) is an advanced extension of the Lubby2 material model, initially developed by Lux (1983) at the Institute of Geotechnical Engineering, Division of Underground Construction, Leibniz University Hannover. The Lubby2 model is fundamentally based on the Burgers rheological framework and characterizes the undamaged (damage-free) creep behavior of rock salt using stress- and temperature-dependent parameters.

In Lubby-CF, the total inelastic strain rate is composed of three distinct contributions: the undamaged (intrinsic) creep component, creep associated with mechanical damage (shear and tensile), and a healing-related creep term (Eq. 1).

$$\dot{\epsilon}^{\text{inel}} = \dot{\epsilon}_{eq}^{cr} \cdot \frac{\partial \sigma_{\text{dev}}^{cr}}{\partial \underline{\sigma}} + \dot{\epsilon}_{eq}^{\omega_{sh}} \cdot \frac{\partial \sigma_{\text{dev}}^{\omega_{sh}|_f}}{\partial \underline{\sigma}} + \dot{\epsilon}_{eq}^{\omega_{te}} \cdot \frac{\partial \sigma_{\text{dev}}^{\omega_{te}}}{\partial \underline{\sigma}} + \dot{\epsilon}_{eq}^{h} \cdot \frac{\partial \sigma_{\text{dev}}^{h|_f}}{\partial \underline{\sigma}} \,. \quad (1)$$

The description of damage-free creep strains from dislocation mechanisms is based on the Lubby2 material model and considers transient and steady-state creep behaviour in an additive manner. The equation of motion for the effective creep rate, $\dot{\epsilon}_{eq}^{cr}$ is defined as follows:

$$\dot{\varepsilon}_{eq}^{cr} = \frac{3}{2}\left(\frac{1}{\bar{\eta}_K\left(\sigma_{eq}^{cr}, T\right)} \cdot \dot{\varepsilon}_{tr}^{\mu} + \frac{1}{\bar{\eta}_M\left(\sigma_{eq}^{cr}, T\right)}\right) \cdot \frac{\sigma_{eq}^{cr}}{1-\omega} \tag{2}$$

The second term describes steady-state or secondary creep based on the stress- and temperature-dependent formulated Maxwell viscosity parameter $\bar{\eta}_M$.

An exponential function describes the dependence of the stresses. The following formulations are used for the viscosity function:

$$\bar{\eta}_M = \bar{\eta}_M^* \cdot exp\left(m \cdot \frac{\sigma_{eq}^{cr}}{1-\omega}\right) \cdot exp(l_3 \cdot T) \tag{3}$$

In the SMRI research project on the subject of creep behavior under small deviatoric stresses (Lüdeling et al., 2024) in the vicinity of salt caverns, the material model was modified (equation 4):

$$\dot{\varepsilon}_{eq,mod}^{cr} = \frac{3}{2}\left(\frac{1}{\bar{\eta}_M\left(\sigma_{eq}^{cr}, T\right)}\right) \cdot \frac{\sigma_{eq}^{cr}}{1-\omega} + A_0 * \left(\frac{\sigma_{eq}^{cr}}{1-\omega}\right)^{n_0} \tag{4}$$

Via the exponential function $A_0 * \left(\frac{\sigma_{eq}^{cr}}{1-\omega}\right)^{n_0}$ the creep behavior can be adjusted for small deviatoric stresses without requiring a change in creep behavior for higher deviatoric stresses (Figure 2).

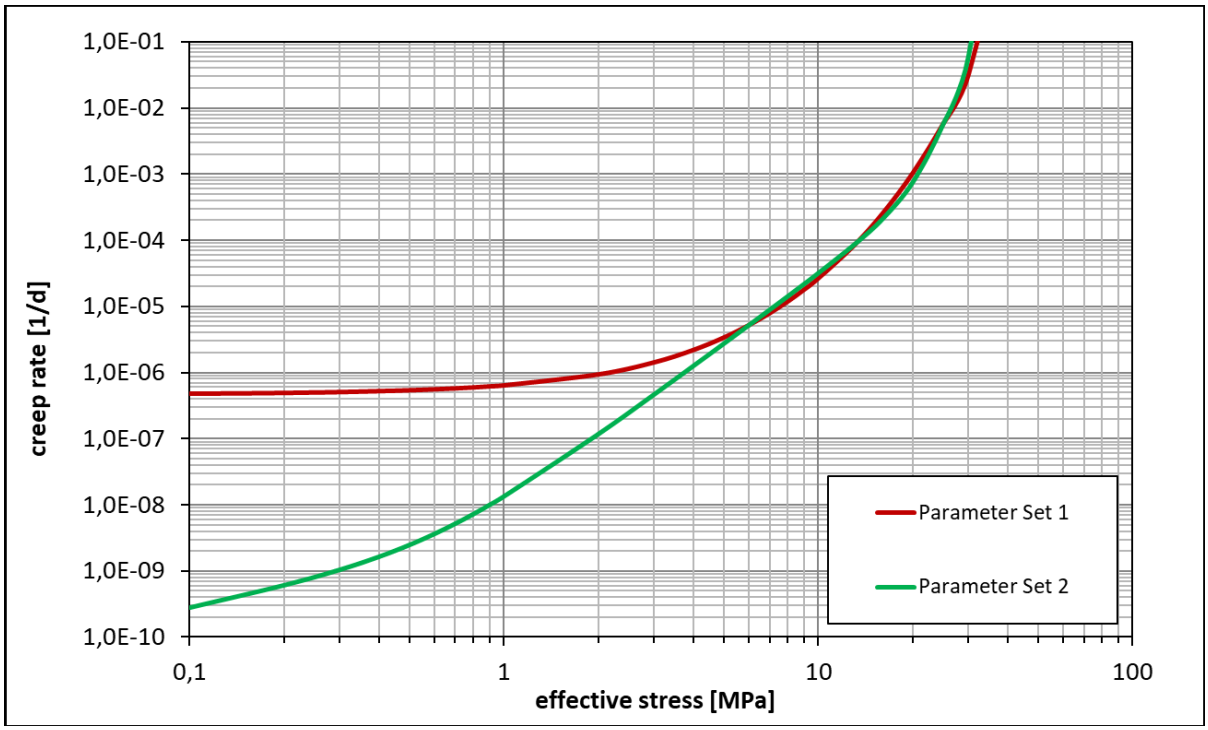

Figure 2. Modified material model Lubby2 // Stationary creep behavior.

When comparing two sets of parameters in the modified Lubby2 material model, it is evident that the creep behavior is nearly identical within a comparative stress range of approximately 8 MPa. This range can usually be reproduced very well in the laboratory as well. More minor deviatoric stresses, on the other hand, can only be reproduced in the laboratory under special conditions, such as high temperatures with a stationary creep rate, as several months or years are required to establish a constant creep rate. To investigate the bandwidth in the stress range below 8 MPa, the material model Lubby2 was modified to accommodate different creep behaviors within this range, while maintaining identical creep properties as those assumed under laboratory conditions.

Within this paper, the Lubby2 model is used, neglecting the damage and healing part. The reason for this assumption is that the focus of the comparison is on the dimensioning of a generic gas storage cavern. If too many parameters were to occur in this comparison, it would be impossible to analyze the stress states between the IGtH-IUB and the Ineris approach.

1.2. Munson-Dawson

The Munson-Dawson (M-D) model (Munson, 1997; Munson et al., 1984, 1993) comprises two differential equations: the strain rate equation, which provides the viscoplastic strain rates, and the evolution equation, which determines the rate of change of an internal variable that describes the transient creep rate. A simplified version of the Munson-Dawson law can then be written as follows:

$$\dot{\varepsilon}_{ij}^{vp} = \frac{\partial \sigma}{\partial \sigma_{ij}} F \dot{\varepsilon}_{ss} \qquad \begin{cases} F = e^{\Delta\left(1-\varsigma/\varepsilon_t^*\right)^2} & \text{when } \varsigma \le \varepsilon_t^* \\ F = e^{-\delta\left(1-\varsigma/\varepsilon_t^*\right)^2} & \text{when } \varsigma \ge \varepsilon_t^* \end{cases} \tag{5}$$

$$\dot{\varsigma} = \left(F-1\right)\dot{\varepsilon}_{ss} \qquad \dot{\varepsilon}_{ss} = A\exp\left(-Q/RT\right)\sigma^n \tag{6}$$

$$\sigma = \sqrt{3J_2} \qquad J_2 = \frac{1}{2} s_{ij} s_{ij} \qquad \varepsilon_t^* = K_0 e^{cT} \left(\sigma/\mu\right)^m \tag{7}$$

$$\mu = E/2\left(1+\nu\right) \text{ and } \Delta = \alpha_w + \beta_w Log_{10}\left(\sigma/\mu\right) \tag{8}$$

This simplified version of the law has 9 parameters: $A, n, Q/R, m, K_0, \alpha_w, \beta_w, \delta$ and c. . The set of parameters considered is taken from Brouard & Bérest (2022). For the calculations in this paper, the Munson-Dawson constitutive model was employed by Ineris in the 2D version of LOCAS (Brouard et al., 2021, 2022) for comparison purposes.

2. Benchmark calculations

2.1. Calculation model

The mechanical stability of salt caverns for Underground Gas Storage is primarily governed by creep deformation, stress redistribution, and thermo-mechanical transients induced by pressure and temperature cycling. To investigate these mechanisms under realistic conditions, this study benchmarks two contrasting geological contexts: domal salt and bedded salt, using advanced constitutive models to evaluate cavern convergence, stress paths, wall displacements, and thermal effects. To ensure consistency and reproducibility, two generic cavern configurations were developed to represent typical Underground Hydrogen Storage (UHS) conditions while retaining the key physical and geometric characteristics of field-scale caverns. This approach enables a direct comparison of constitutive laws and numerical approaches, covering the two main operational contexts observed worldwide: large, high-volume caverns in homogeneous domal salt and smaller, thinner caverns in stratified bedded formations with more complex rheology.

Both caverns share a vertical cylindrical geometry with half-ellipsoidal terminations at the roof and bottom (see Figure 3). The domal salt cavern is the larger configuration, with a free volume of 831,344 m³ (5,228,996 bbls), a height of 335 m (1,100 ft), and a maximum diameter of 61 m (200 ft). Its center lies at an average depth of 1,082 m (3,551 ft), and the last cemented casing shoe is set at 914 m (2,999 ft). In contrast, the bedded salt cavern is more compact, with a free volume of 297,411 m³ (1,870,659 bbls), a height of 153 m (501 ft), and the same average diameter of 61 m (200 ft). It is located at an average depth of 1,082 m (3,551 ft), with the casing shoe positioned at a deeper depth of 1,005 m (3,298 ft). At both sites, the geothermal gradient produces a temperature of approximately 40 °C (104 °F) at the cavern mid-depth. In the LOCAS simulation, the caverns are predominantly filled with hydrogen gas, accounting for more than 99% of the total free volume in the bedded configuration and 84% in the domal configuration. A brine sump is located at the bottom of the caverns.

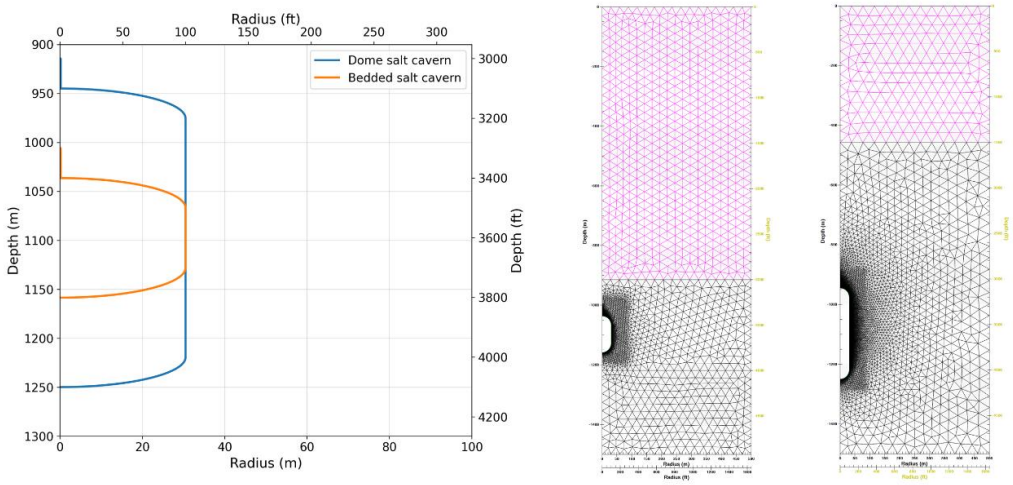

Figure 3. Cavern shape and mesh for benchmark calculations.

2.2. Initial and boundary conditions

The simulations were performed using LOCAS and FLAC3D, enabling a direct benchmark of advanced constitutive laws, including the Munson–Dawson viscoplastic creep law and the Lubby2 model.

The numerical analyses were carried out under boundary and loading conditions designed to replicate site-specific geology and operational scenarios. The geostatic stress field was derived from overburden and

salt density profiles, while the thermal field incorporated a depth-dependent geothermal gradient to capture realistic *in-situ* temperature distributions. For the analysis, the overburden density is assumed to be 2,100 kg/m³ (131 lb/ft³), and the salt density is assumed to be 2,180 kg/m³ (136 lb/ft³). The pressure history captured the full operational envelope of the storage system, with the maximum pressure limited by the lithostatic margin, corresponding to a gradient of 0.18 bar/m (0.79 psi/ft) at the casing shoe. The minimum pressure was maintained at a gradient of 0.05 bar/m (0.22 psi/ft) to ensure cavern stability. Cyclic injection and withdrawal rates were defined to replicate realistic field-scale hydrogen storage operations, ensuring that the simulated loading conditions accurately represented operational cycling scenarios. The computational mesh in LOCAS employed a 2D axisymmetric configuration to strike a balance between computational efficiency and resolution, featuring fine refinement zones around the cavern wall, roof, and wellbore to capture sharp stress and deformation gradients (0.2 m at cavern wall), and coarser meshing in the far field to minimize computational cost (see, Djizanne et al. 2023a,b, 2024, 2025; Djizanne & Brouard 2025). The axisymmetric finite element models were configured for both bedded salt and domal salt geological settings, extending 1,600 m (5,249 ft) radially and 2,000 m (6,562 ft) vertically to minimize boundary effects on cavern-scale responses.

- In the bedded salt configuration, 914 m (2,999 ft) of overburden sediments overlay a 300-meter-thick halite layer that contains the cavern. At the average cavern depth of 1,082 m (3,551 ft), the geostatic pressure reaches 224 bar (3,249 psi), and at the casing shoe depth of 1,006 m (3,299 ft), it is 208 bar (3,016 psi). The geothermal gradient yields an *in-situ* temperature of 40 °C (104 °F) at cavern depth, with surface ground temperatures of around 10 °C (50 °F).
- In the domal salt configuration, a thin 457 m (1,499 ft) overburden covers a massive, homogeneous halite dome. At the average cavern depth of 1,082 m (3,551 ft), the geostatic pressure is 228 bar (3,306 psi), and at the casing shoe depth of 914 m (2,999 ft), it is 192 bar (2,786 psi). The geothermal profile yields similar thermal conditions, with a temperature of 40 °C (105 °F) at the cavern depth.

Boundary conditions were applied to simulate geostatic stress along the lateral boundaries and zero vertical displacement at the model base. Meanwhile, the cavern walls were subjected to internal pressure and temperature variation resulting from cyclic operations. This setup enabled accurate simulation of stress redistribution, cavern convergence, creep deformation, and thermal-mechanical coupling over operational time scales.

IGtH-IUB performed a numerical calculation using a coupled thermo-mechanical approach with a numerical model of a quarter in the Finite Difference Code (FDM) FLAC3D. Figure 4 shows the computational model. Visible here are the cavern, the parts of the neck, the roof section, and the cylindrical part. A finer mesh was implemented in the upper part to study the infiltration fracture process during the calculation of the design load case for this cavern. The reason for creating a finer mesh only in this part of the cavern is that, on the one hand, this is the part of the cavern wall where fractures occur first, and it also saves calculation time.

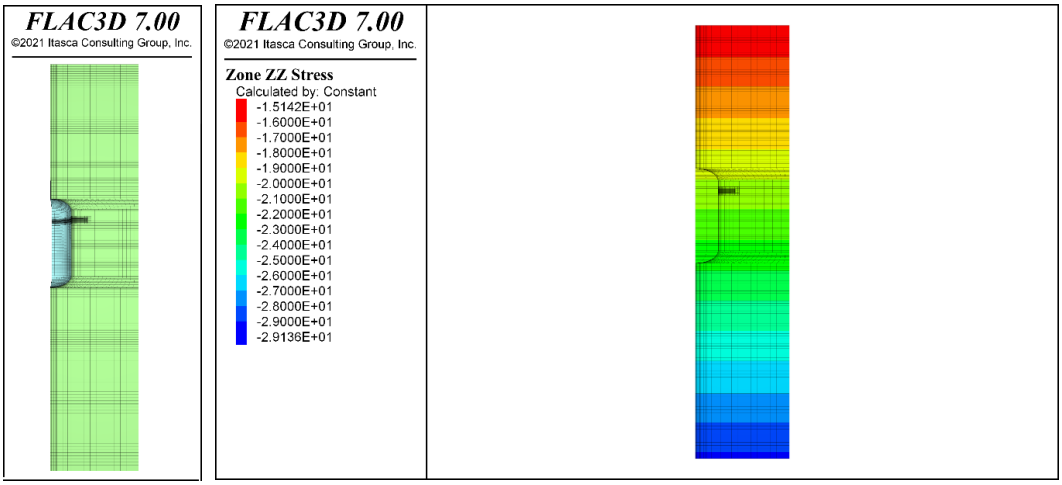

Figure 4. Calculation Model and primary stress state (σ_{zz} in MPa).

3. Ineris computation results

3.1. Temperature evaluation

Thermal effects in gas storage caverns have long been recognized as a critical factor in rock mechanics analysis and design methodologies. Ignoring the interaction between temperature variations and the stress state at the cavern wall and in the surrounding salt is no longer acceptable in modern stability assessments. In this study, both modeling frameworks consider these thermal effects. Ineris uses the LOCAS software, which integrates the calculation of thermal state variables directly into the mechanical solver for fully coupled thermo-mechanical simulations. IGtH-IUB employs the KAVPOOL (ESK) thermal simulator to generate temperature profiles based on representative operational load cases, which are then imported into FLAC3D for coupled thermo-mechanical analyses. This integrated approach ensures that temperature-driven stress redistributions and deformation responses are accurately captured in both modeling workflows. Djizanne et al. (2025) demonstrated that the thermodynamic simulation results obtained by both teams are consistent and comparable, confirming the robustness and reliability of the modeling approaches used in this study.

In Figure 5, the hydrogen temperature rises during injection due to gas compression and then gradually equilibrates toward the brine and rock temperatures through thermal exchange. During withdrawal, the reverse occurs: expansion cooling drives a sharp temperature drop, with transient gradients persisting before stabilization. Brine shows more minor but consistent temperature fluctuations, reflecting its higher thermal inertia. The casing-shoe pressure trace confirms the operational phases and the synchronization between thermal and pressure cycles.

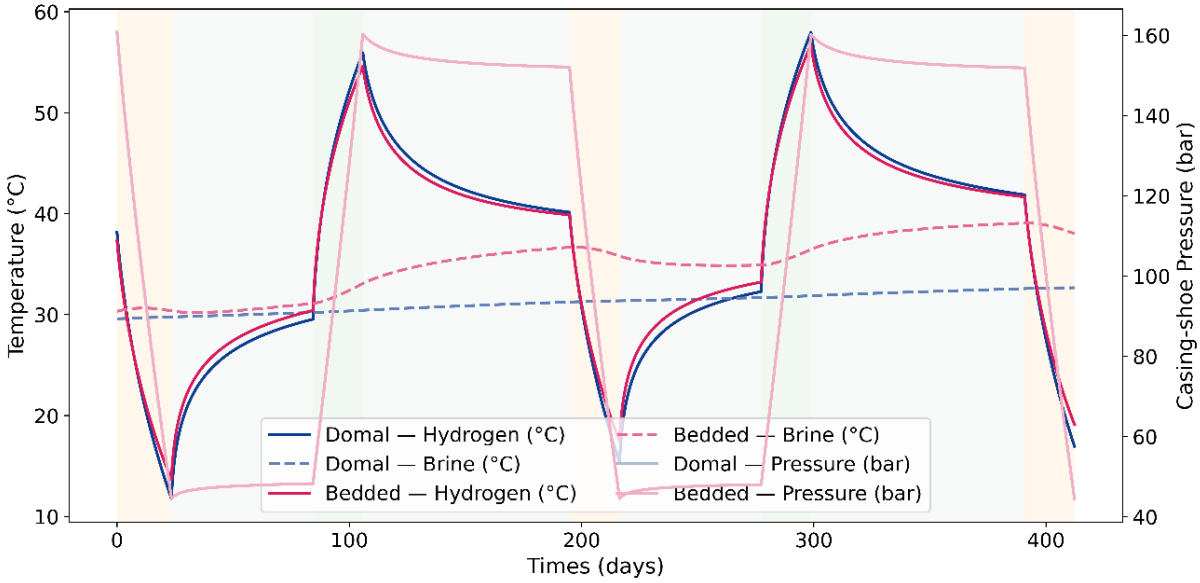

Figure 5. Evolution of cavern temperature and casing-shoe pressure as a function of time (T(°F) = T(°C) * 9/5 + 32) / 100 bar = 1,450 psi).

Figure 6 shows the spatial distribution of temperature within the rock mass at the end of the operational cycle. Near the cavern wall, a thermal transition zone is observed, even if the thermal penetration into the surrounding rock salt is sufficient to drive transient stress redistribution in thermo-mechanical simulations. These localized gradients can alter creep rates and affect interface stresses.

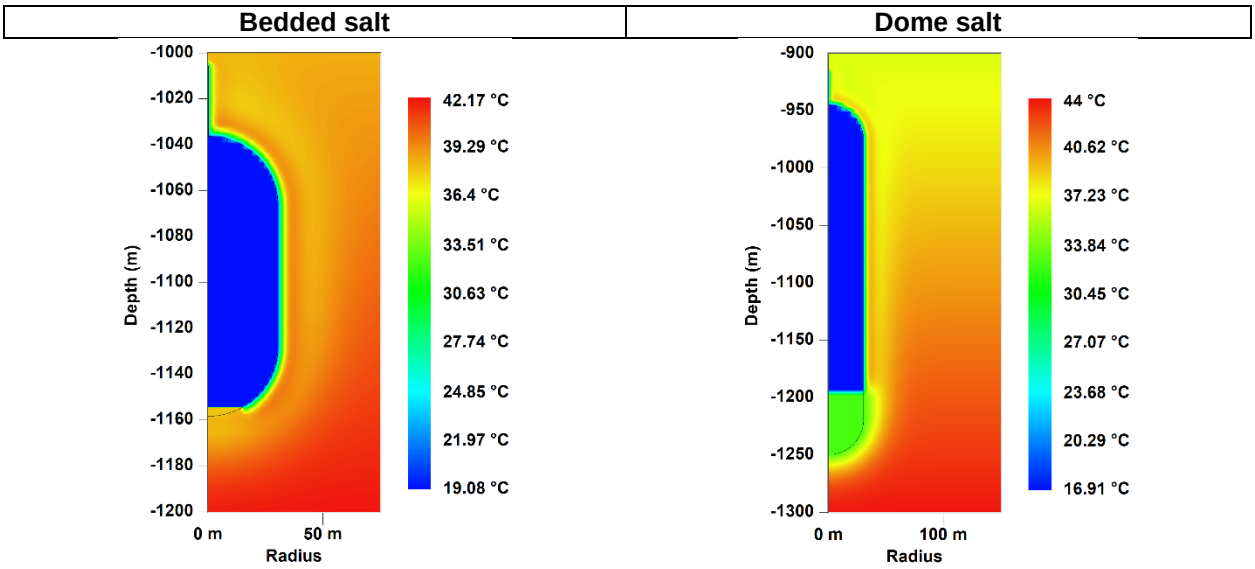

Figure 6. Contours plot of the temperature at the end of the cyclic loading (100 m = 328 ft).

3.2. Convergence and volume loss rate

Figures 7 and 8 illustrate the evolution of cavern volume and the volume-loss rate over time, expressed relative to the initial reference time. Figure 7 shows the relative volume change (ΔV/V). Withdrawal phases amplify creep-driven closure, particularly around the cavern roof and neck, while injection phases temporarily counterbalance closure by increasing internal pressure and reducing deviatoric stress. The domal salt configuration exhibits slightly higher cumulative closure. In contrast, the bedded salt case maintains lower closure rates.

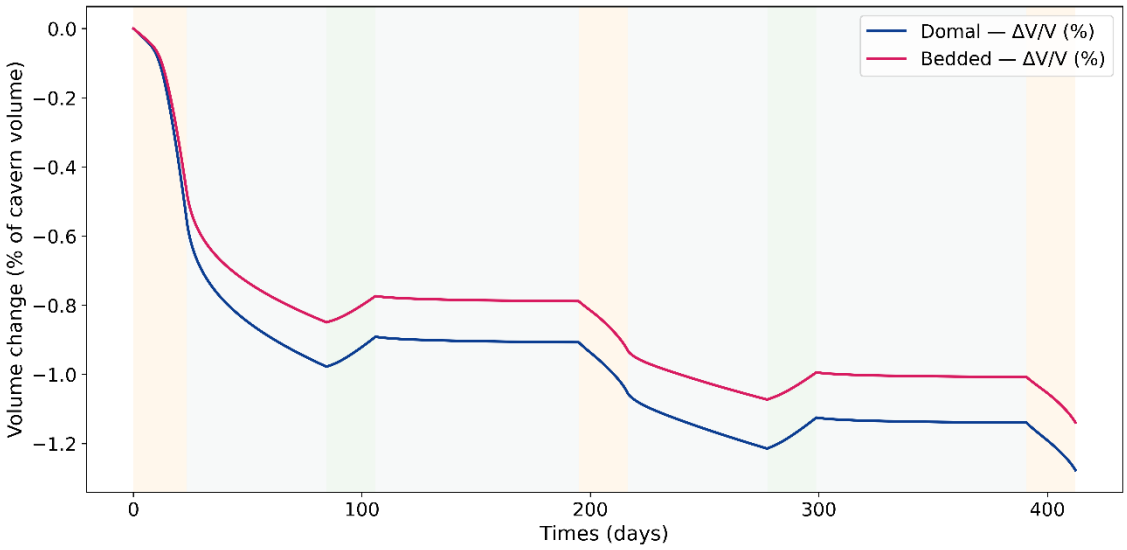

Figure 7. Cavern convergence evolution (% of cavern volume) as a function of time.

Figure 8 presents the cavern volume loss rate (per year). Peaks correspond to operational transitions, with sharp increases at the onset of withdrawal phases. During steady phases, the volume-loss rate stabilizes at low values, typically below 1% per year, which aligns with safe economic targets.

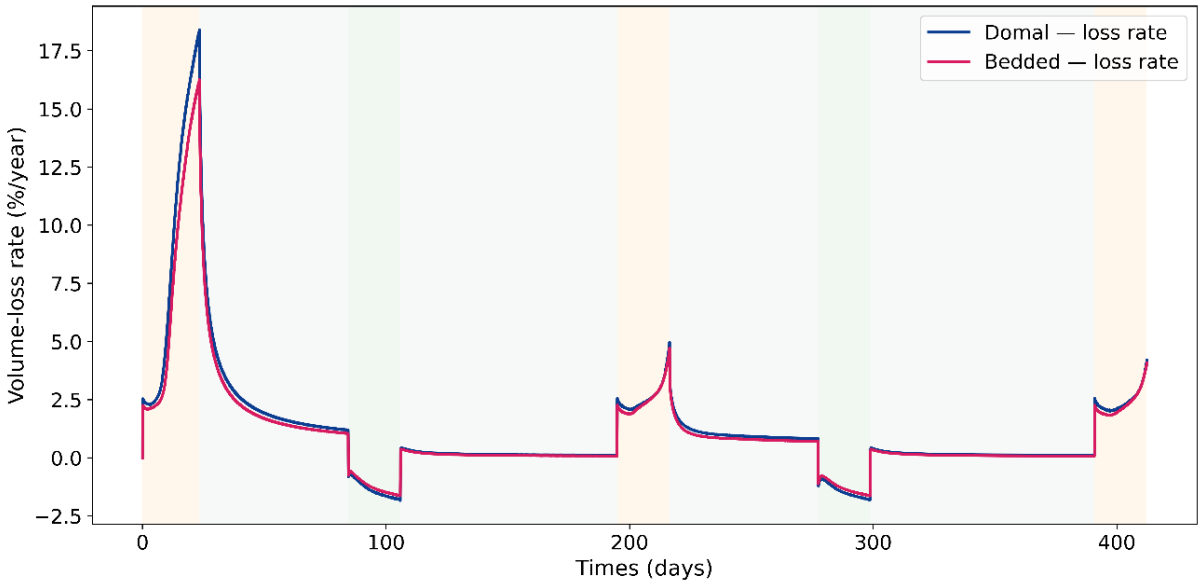

Figure 8. Cavern convergence in cavern volume loss rate as a function of time.

From the following section onward, the time evolutions of the mechanical parameters are evaluated at a monitoring node located in the upper part of the cavern, as indicated in Figure 9.

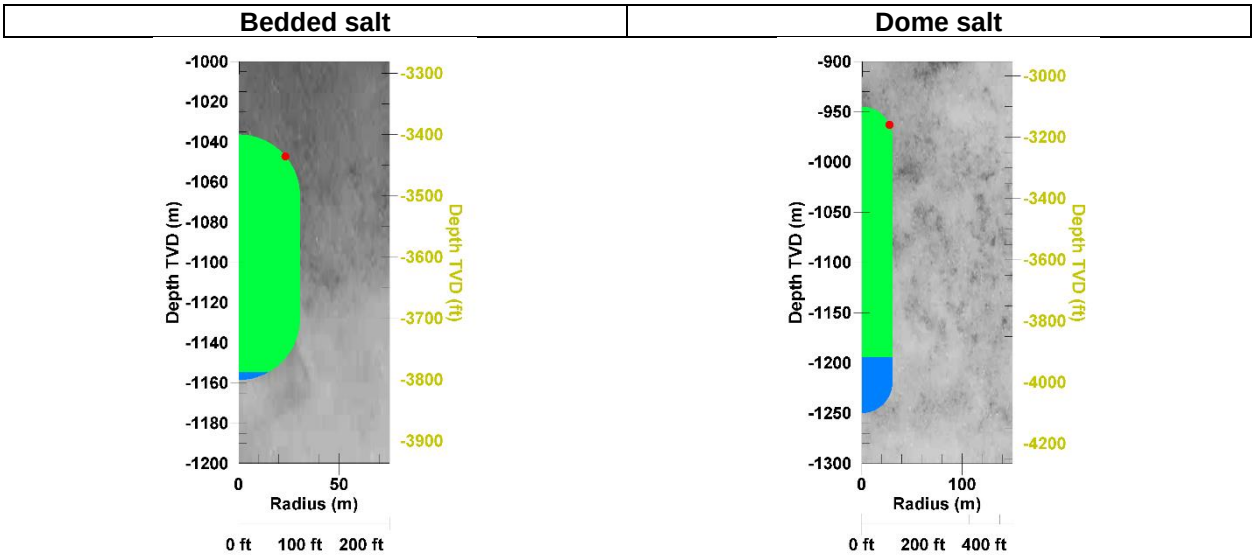

Figure 9. Selected node localized at cavern roof (red point) for both configurations: Bedded salt (-Depth: -1,047 m (-3,435 ft), Radius: 23 m (75 ft)) and Dome salt (Depth: -963 m (-3,159 ft), Radius: 28 m (92 ft)); (100 m = 328 ft).

3.3 Deviatoric stress

The deviatoric stress $\sqrt{J_2}$ represents the intensity of shear stress, while the mean stress $\sigma_m = -I_1/3$ reflects average confinement. Figure 10 shows their evolution and spatial distribution, together with temperature variations, in domal and bedded salt caverns during cyclic operations. Injection phases increase mean confinement and reduce shear intensity near the wall, promoting a more stable stress state. In contrast, withdrawal phases reduce confinement and elevate shear demand, driving the system closer to critical

conditions, particularly in bedded salt. Withdrawal phases reduce mean confinement σ_m and amplify shear demand $\sqrt{J_2}$, pushing the stress state closer to dilatancy or tensile damage thresholds, especially in the bedded salt case study. Temperature fluctuations follow pressure cycles: rapid depressurization drives cooling of hydrogen and brine, transiently modifying viscosity and redistributing stress. These thermal transients are more pronounced in bedded salt case study.

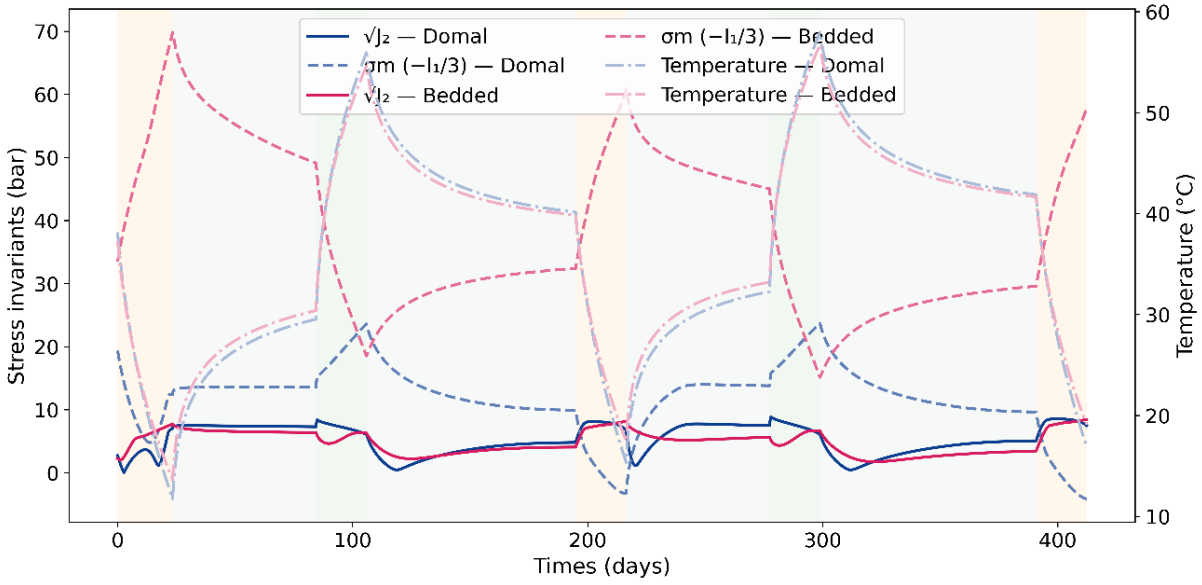

Figure 10. Evolution of the stress invariants with temperature in the upper part of the caverns.

Figure 11 confirms these trends. Near-wall shear zones (high $\sqrt{J_2}$) develop during withdrawal phases, with bedded salt showing broader and more intense shear bands, indicating a higher risk of damage initiation. Domal salt case study exhibits a more confined and homogeneous response.

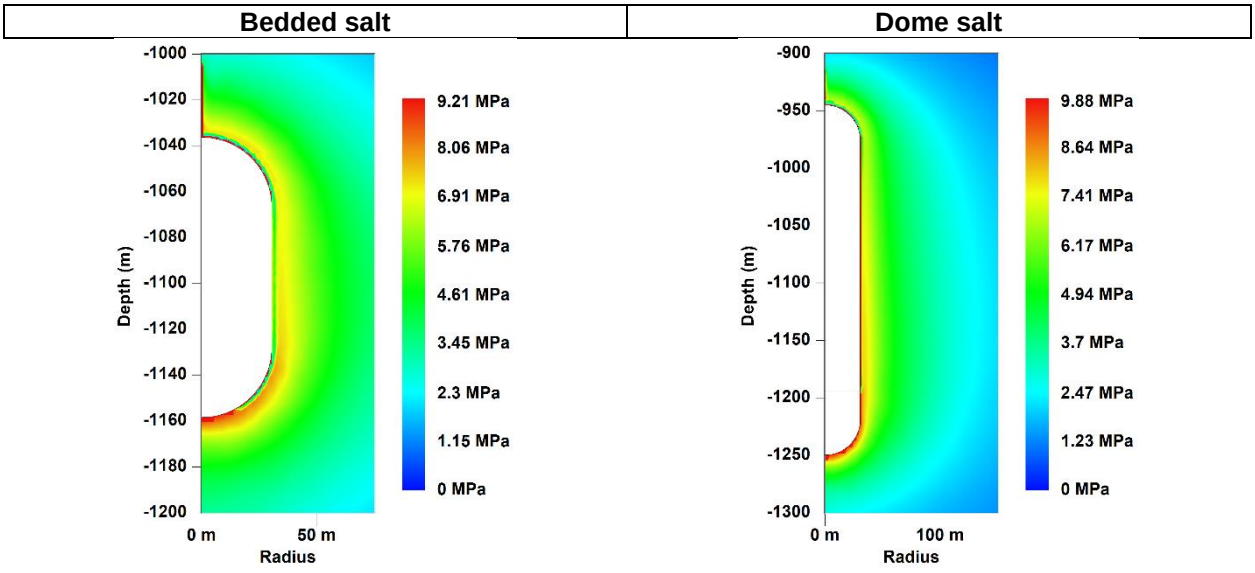

Figure 11. Contours plot of the deviatoric stress for both cases (100 m = 328 ft).

Figure 12 illustrates the evolution of the principal stresses (σ_1: most compressive, σ_2: intermediate, σ_3: least compressive) in domal and bedded salt caverns during pressure cycling.

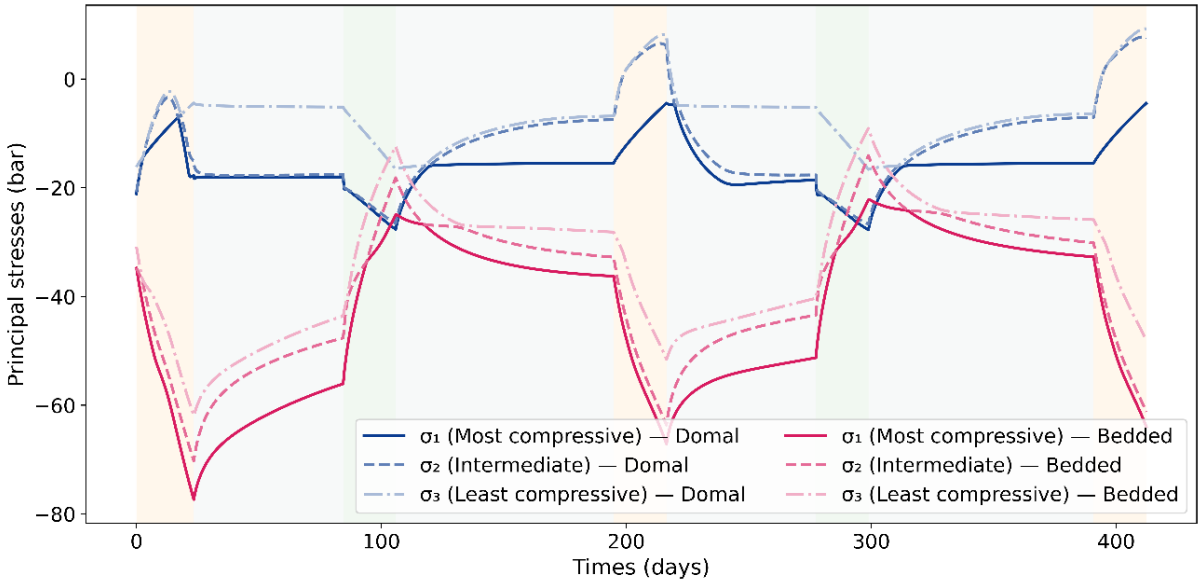

Figure 12. Evolution of the principal stresses as a function of time for both scenarios.

During injection phases, the stress state in both caverns becomes more favorable: the most compressive principal stress (σ_1) decreases, the least compressive stress (σ_3) becomes less compressive, and the radial stress (σ_{rr}) relaxes under internal pressure support, collectively reducing deviatoric demand and mitigating the risk of tensile spalling or shear-related damage. In contrast, withdrawal phases drive σ_1 upward and bring σ_3 closer to zero, while the tangential (σ_{tt}) and vertical (σ_{zz}) components become more compressive, amplifying deviatoric stresses and shifting the stress path toward less stable conditions (See Figure 13). This amplification is more pronounced in the bedded salt cavern, where the wider σ_1–σ_3 spreads and larger σ_{tt} excursions could reflect mechanical anisotropy and layered heterogeneity, making the formation more sensitive to cyclic loading and more susceptible to microcracking and spalling than the domal salt case.

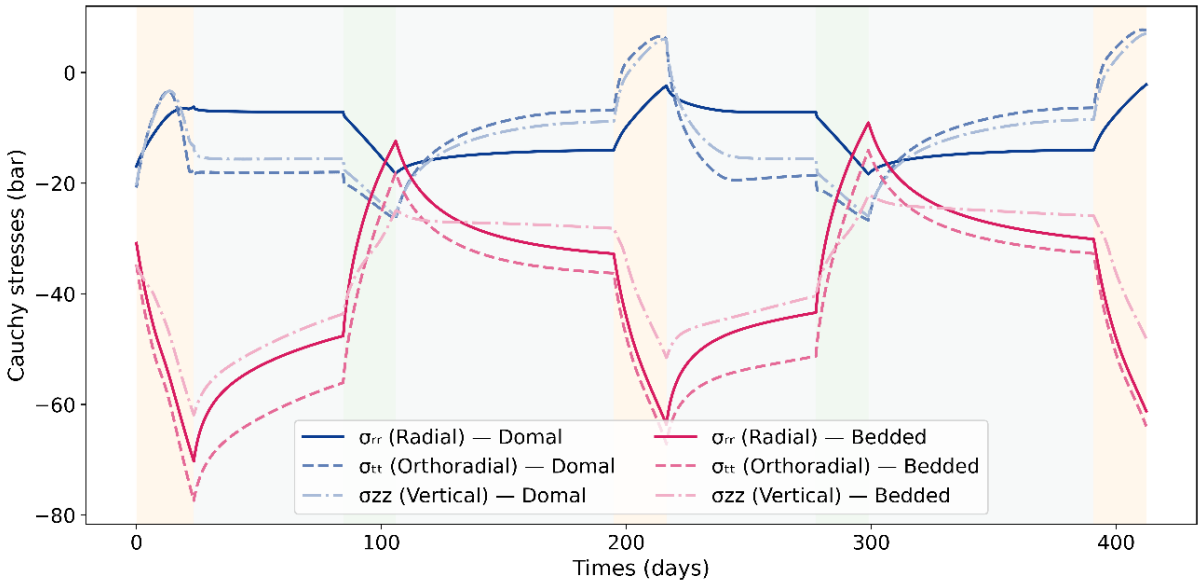

Figure 13. Cauchy stress components as a function of time.

3.4 Bérest effective stress at maximum pressure

At maximum operating pressure (day 390), cavern stability is assessed with the no-tensile Bérest effective stress criterion (Brouard et al., 2007; Djizanne et al., 2012), which requires the least compressive principal stress at the wall plus the internal hydrogen pressure to remain below the salt tensile strength (i.e., $\sigma_3 + P_c < T_{salt}$). Figure 14 maps the resulting Bérest effective stress, where magenta contours indicate locations where the state becomes tensile and the criterion is potentially violated. The bedded-salt case exhibits a broader, deeper tensile reach in the roof and along the sidewall, indicating higher susceptibility to tensile damage; the domal-salt case shows a narrower, more localized tensile band confined near the wall.

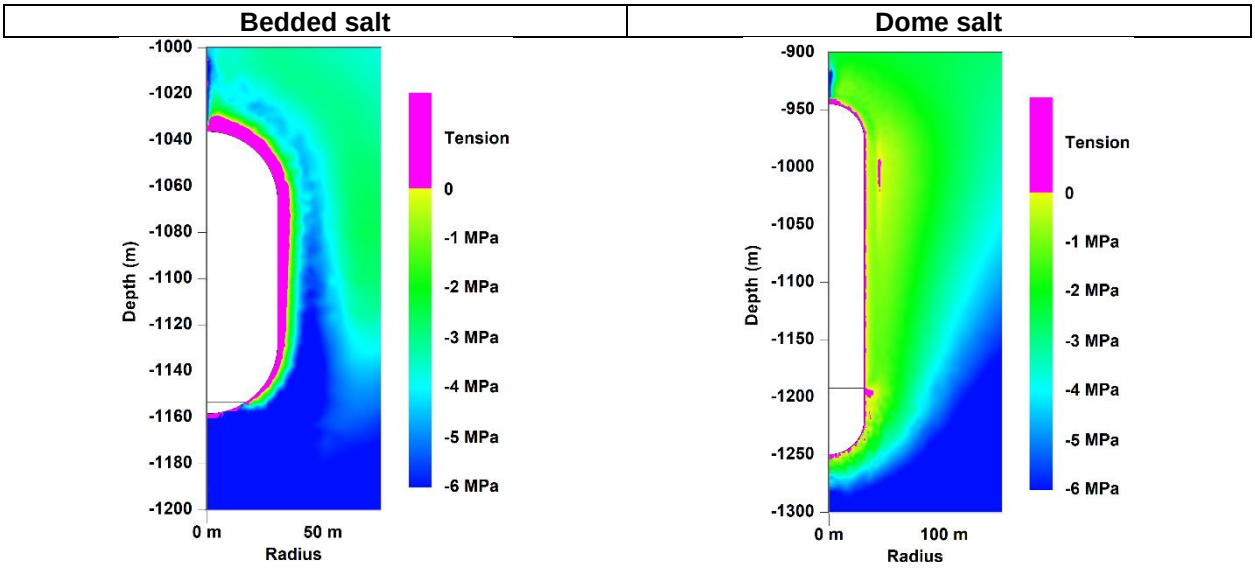

Figure 14. Bérest effective stress around the salt cavern at maximum pressure (390 days). The damaged area is outlined in magenta.

3.5 Radial and vertical displacements

Figure 15 shows the radial and vertical displacements of the cavern roof under the combined effects of creep deformation and pressure cycling.

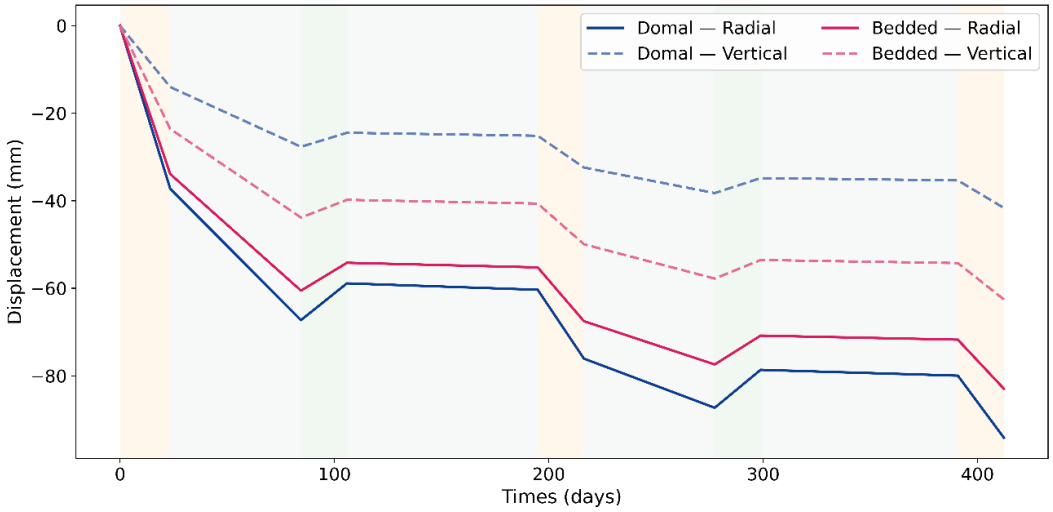

Figure 15. Radial and vertical displacements in both cases.

The radial displacement evolves more rapidly during each operational phase, reflecting the localized creep closure of the cavern walls. In contrast, vertical displacements exhibit a slower but more cumulative response, consistent with broader stress redistribution within the roof beam and underlying salt layers. The bedded salt case shows greater vertical displacement amplitudes compared to the domal configuration. These larger vertical motions may contribute to elevated strain levels at the well-casing interfaces, with implications for casing shoe integrity and long-term well stability.

3.6 Factor of safety

Dilatancy marks the onset of salt damage, where microcracking develops without macroscopic failure, leading to increased permeability, reduced sound velocity, elevated acoustic emissions, and accelerated deformation (Chan et al., 1994). This behavior is quantified through a factor of safety (FoS), which must remain strictly greater than one to ensure stability, based on the dilatancy criterion of DeVries et al. (2005). As shown in Figure 16, zones with magenta color ($FoS \leq 1$) indicate entry into the dilatant regime. In the bedded salt cavern case study, this zone is thicker and more extensive around the cavern wall. In contrast, the domal salt cavern case exhibits a thinner and more localized dilatant band, consistent with the possible homogeneous and isotropic response of massive halite.

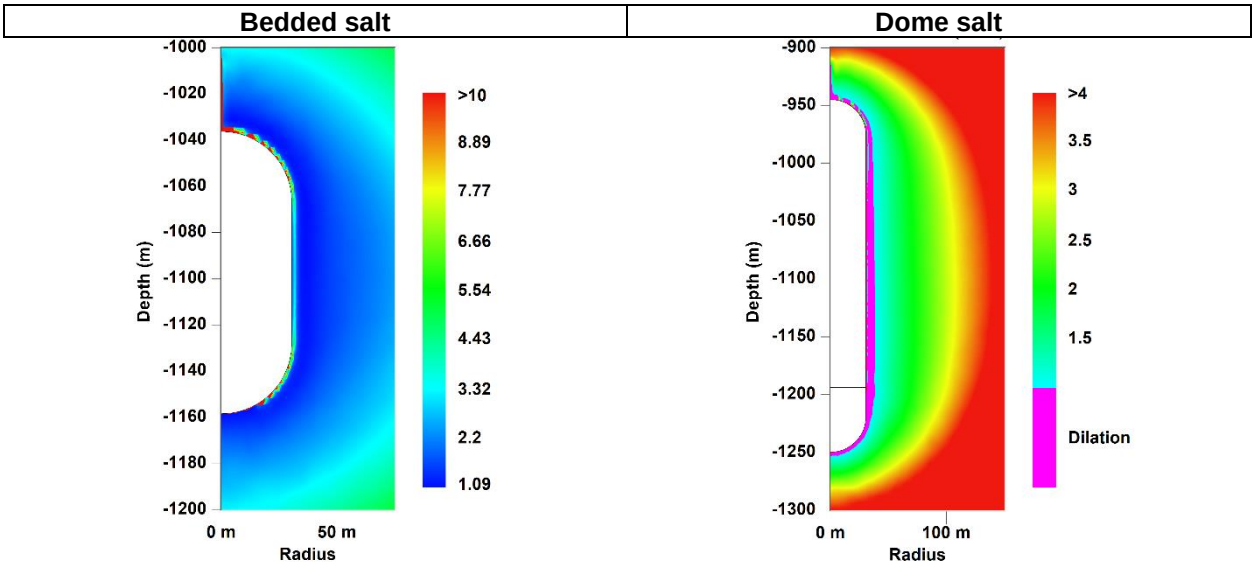

Figure 16. Factor of safety for both cases - Salt dilates in the area marked in magenta.

This study demonstrates distinct mechanical responses of domal and bedded salt caverns case studies under hydrogen storage conditions. Domal salt case exhibits lower convergence, more stable stress redistribution, and reduced thermo-mechanical sensitivity, consistent with its possible homogeneous and stronger nature, as seen in massive halite. The results align with established mechanical stability criteria. Maintaining the Bérest effective pressure below the tensile strength threshold mitigates the risk of fracturing and permeability increases, while keeping the minimum pressure above the dilatancy threshold ($\sqrt{J_2} < \sqrt{J_{2,\text{dil}}}$) preserves tightness and structural integrity. Cycling analysis reveals that rapid depressurization and high-frequency operations exacerbate stress and thermal gradients, thereby increasing the risk of fatigue and damage, particularly near the casing shoe. Accurate site-specific rheological calibration and coupled thermo-hydro-mechanical (THM) simulations are crucial for capturing the interplay between creep, stress redistribution, and thermal effects. Field data (pressure, temperature, sonar surveys, and acoustic emissions, etc.) provide critical feedback for refining these models, where possible heterogeneity can amplify stress and deformation, conservative operational envelopes and continuous monitoring of stress indicators, displacement, and volume-loss rates (<1%/year) are required to limit long-term damage and cumulative creep (<10%).

4 Calculation results (IGtH-IUB)

4.1 Maximum allowable pressure

Two different types of failure can basically describe the loss of operational functionality under maximum pressure conditions:

- The sudden fracturing of the rock is accompanied by the development of macro-fractures, associated with the loss of gas along these newly created pathways and with a potentially progressively extending fracture.
- The infiltration of the gas into the rock mass begins at internal cavern pressures below that which would lead to the above-described macro-fracturing.

To avoid the risk of fracturing the rock mass, the maximum pressure gradient *G* is restricted to a level below the gradient/internal pressure derived from the lower limiting case of the measured rock mass densities. As a criterion for the safety against gas leakage due to infiltration, at the calculated time when the pressure is raised to the maximum internal cavern pressure level, it is necessary that:

- A sufficiently large safety zone (thickness of a_{exist}) is available around the cavern in which the differences between the principal stress components σ_2 or σ_3 and the internal pressure pi remain below a limiting value (Figure 17), and that.
- The casing shoe zone is, at the same time, sufficiently embedded within this safety zone.

Figure 17 shows the effective tangential stress ($\sigma_{t\,eff}$) minus the current cavern gas pressure (p_o), which should be smaller than a location-specific threshold value ($\sigma_{t\,eff*}$). The safety zone that forms (a_{exist}) should also be larger than a location-specific limit value (a*). Regarding the design of the maximum internal cavern pressure, experience has shown that considering thermodynamic processes is of secondary importance. Temperature changes do not significantly impact the formation of safety zones in the cavern roof area of a gas storage cavern. Various benchmark calculations have demonstrated that the temperature influence does not extend into the safety-relevant rock mass area (Zapf et al., 2019).

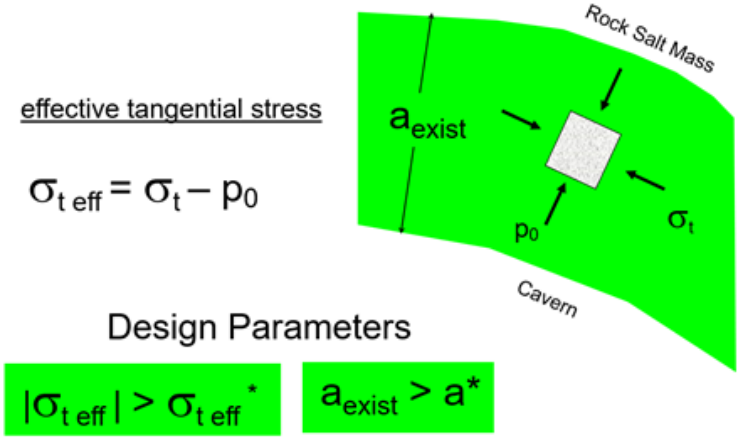

Figure 17. Rock mechanical design criteria for maximum cavern gas pressure (Rokahr et al., 1997).

Figure 18 illustrates, for the example calculations in this paper, the distribution of safety zones at the roof of the cavern, where the relevant principal stress components exceed the internal pressure. In the assessment for dimensioning a gas storage cavern, the IGtH-IUB approach considers the differences between σ_2 and σ_3 with respect to the internal pressure. The experience at IGtH-IUB of assessing many caverns shows that the relevant stress component is σ_2-pi for a conservative design of maximum pressure. In that case, the width of the safety zones around the cavern in the roof section is smaller than the zones for σ_3-p_i. The value of p_i is equal to p_o.

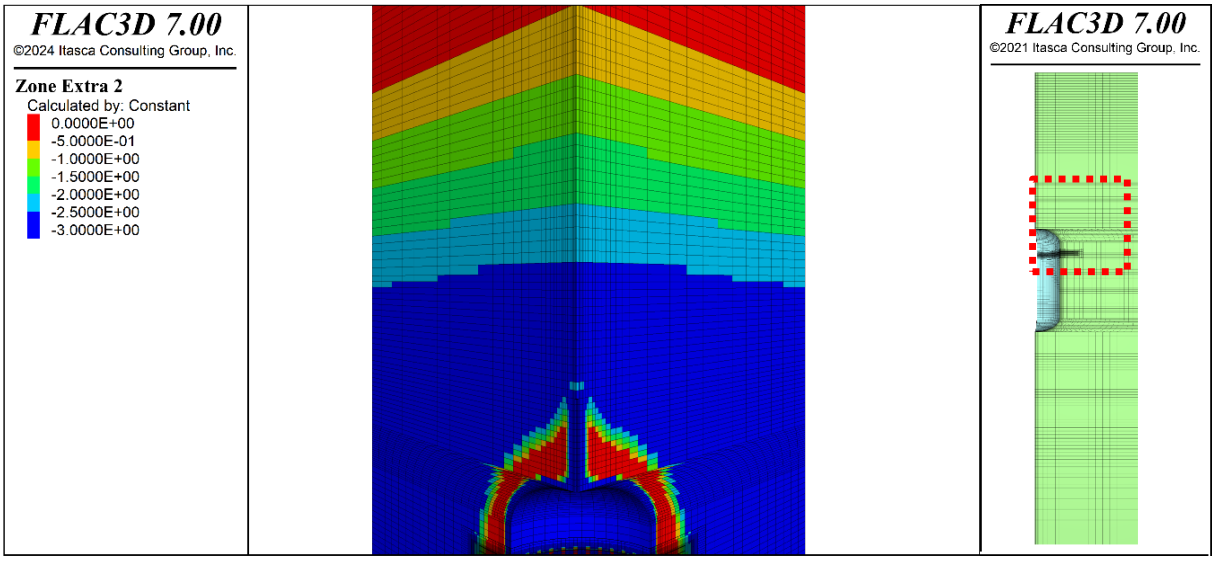

Figure 18. Assessment of maximum pressure (σ_2 – p_i in MPa).

The demand under these internal pressure conditions is that the relevant orthogonal component to the internal pressure-directed principal stress is -2.5 MPa, which is larger than the internal pressure in the cavern. The safety zone should have a size of at least 25 m (82 ft) in thickness, as per this example (location-specific assessment). With a maximum pressure of 16 MPa (2,323 psi) in this example, the safety requirements are fulfilled.

4.2 Minimum pressure

The stress intensity index (Rokahr & Staudtmeister, 1993) is used for the determination of the minimum pressure and is defined as the ratio between the existing stress of the material and the deviatoric stress of the material, which can be accommodated in the short term:

$$\eta = \frac{\sqrt{2J_2^D}_{vorh}}{\beta^D(\underline{\sigma})} \tag{9}$$

intensity where

J_2^D: second invariant of the deviator of the local stress tensor, i.e., at the cavern wall.

β^D: short-term failure strength of material determined from the results of laboratory tests, depending on the stress state $\underline{\sigma}$.

Empirically, the failure strength of rock salt diminishes with the duration of the stress. Reductions in the short-term strength are necessary for very long time periods (permanent strength). The required minimum internal cavern pressure is determined based on maintaining the integrity of the perimeter, i.e., avoiding any spalling from the cavern wall, which would increase the diameter of the cavern.

The verification of perimeter integrity is undertaken based on the following evaluation criteria, which are also applied to the results of numerical calculations, using location-specific limits. In the following, η the stress value is always the same, only with different indices (G = maximum short-term strength, D = fatigue strength, PK = pillar core area). Verification that the short-term maximum stress intensity index η_{IUB} is limited to $_{max}\eta_G$ after Eq. 10:

$$\eta_{IUB} \leq {}_{max}\eta_G \tag{10}$$

$_{max}\eta_G$ is set at 50 % for the minimum internal cavern pressures investigated here. For simplicity, the fatigue strength and pillar core area are not discussed in this paper.

Figure 19 shows the stress distributions versus radius at the reference depth (red dotted line at 2/3 of the cavern height) for the three stress components and the stress intensity index.

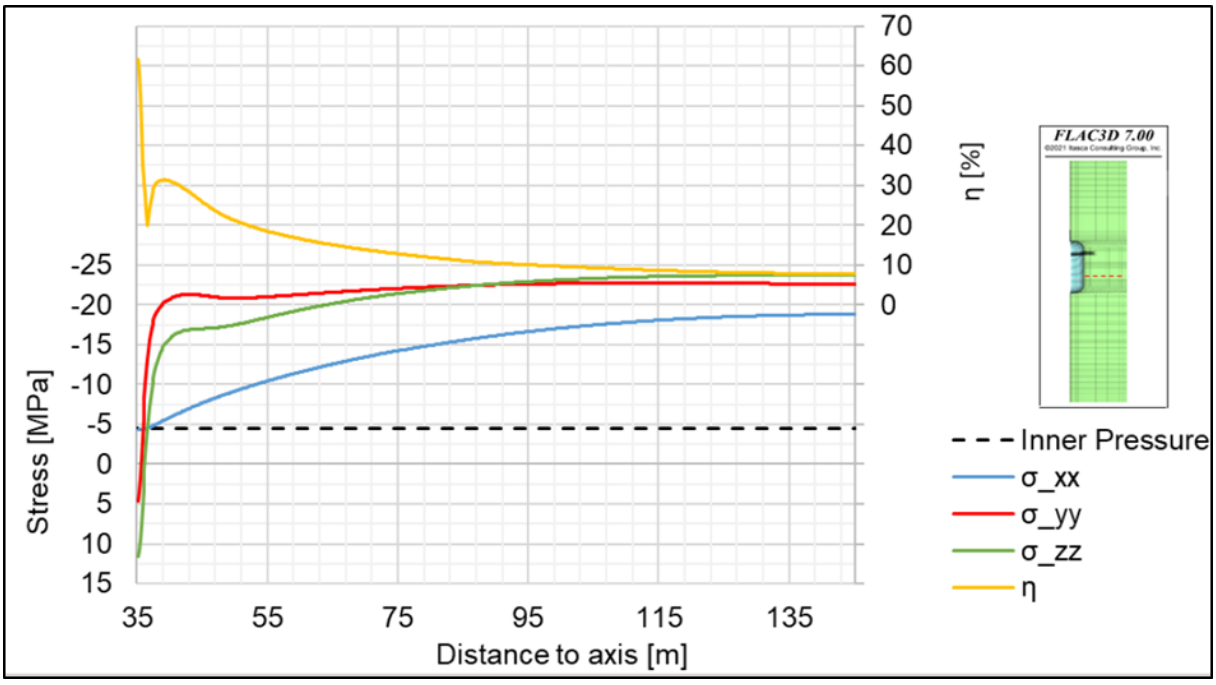

Figure 19. Assessment of minimum pressure (σ/η_{IUB} vs. distance to cavern axis) / 100 m = 328 ft.

In this example, it can be seen that the stress intensity index at the cavern wall exceeds the rock mechanical limit, which is set at 50% in the design concept. The reason for this is that at the cavern wall, both the circumferential and vertical stress components show tensile stresses, which cause J_1 to be invariant to very low values.

$$J_1 = \sigma_1 + \sigma_2 + \sigma_3 \tag{11}$$

This ultimately leads to a large stress intensity index when correlating J_1 with the deviatoric stress σ_v.

In the case of this stress state, an infiltration fracture would occur at the reference depth. This would lead to a change in the stress intensity index. When determining the minimum pressure for such a cavern, slower withdrawal rates should be considered to avoid the occurrence of tensile stresses at the minimum pressure level (most of the time, traction occurs before reaching the minimum pressure), because the temperature difference between the maximum and minimum internal pressure is dependent on the gas withdrawal rate. The higher the withdrawal rate is, the larger the temperature drop. This leads to temperature-induced stresses that show high tensile stresses (Voegeli, 2024).

4.3 Maximum permissible operation rates

Infiltration fractures are to be expected at the cavern wall if one of the principal stress components has a compressive stress value in the range of $\Delta\sigma$ = 1-2 MPa, smaller than the radial stress component or than the prevailing internal pressure due to the cooling during withdrawal phases in salt caverns (Zapf, 2012; Yildirim, 2018, 2019). An example of the stress state at the cavern wall during a design load case is given in Figure 20:

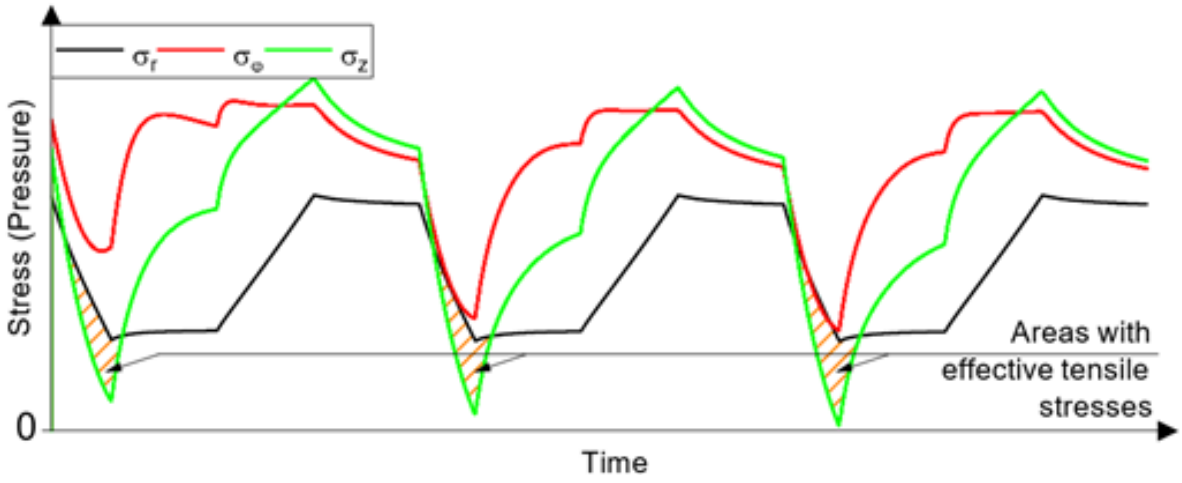

Figure 20. Stress vs. time for a thermo-mechanical calculation of a design load case (DLC) at the cavern wall. Orange stripes indicate areas of (effective) tensile stresses.

The diagram in Figure 20 illustrates the three Cauchy stress components, σ_r (black line), σ_φ (red line), and σ_z (green line), for a point on the cavern wall over time in a thermo-mechanical numerical calculation. The radial stress component σ_r is equal to the internal pressure p_i prevailing in the cavern. The dimensioning concept assumes that infiltration fractures can develop in the time periods marked with orange stripes. From a rock mechanical perspective, the development of the infiltration fracture should not exceed a few meters into the rock salt mass. The fracture length depends on several factors, including the geometry of the cavern, depth, creep behavior, and operational parameters.

The value of the stress difference given in this paper ($\Delta\sigma$ = 1-2 MPa) was demonstrated in a research project at the University of Hanover (project LARISSA, funded by the Federal Ministry for Economic Affairs and Climate Action) in the laboratory on numerous salt test specimens under different boundary conditions (Baumgärtel et al., 2022). Figure 21 illustrates the development of infiltration fractures within the rock salt mass following the calculation of the design load case.

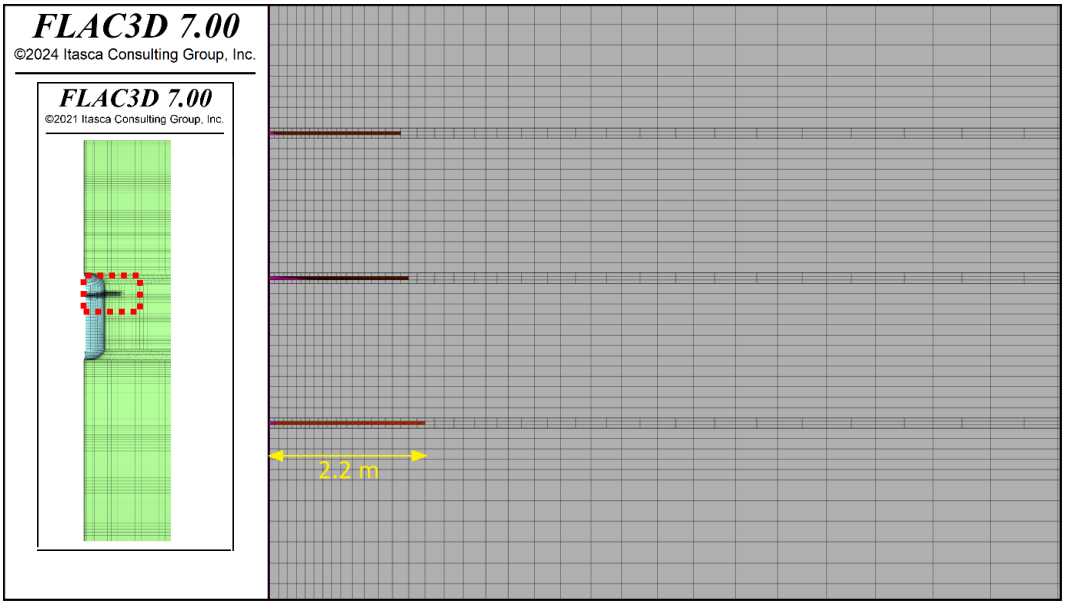

Figure 21. Assessment of infiltration fracture length (2.2 m = 7.22 ft).

After calculating the design load case, the infiltration fracture is evaluated as described in Zapf (2019). The primary factor in the development of a fracture in the rock salt is the cooling during the withdrawal phases, during which tensile effective stresses appear at the cavern wall. In this example, the fracture length was calculated to be 2.2 m (7.22 ft). This length is acceptable from a rock mechanics perspective, given the cavern configuration. The recommendation in this particular case is to limit the operating rate for withdrawal and refilling to 75,000 Nm³/h (471,735.75 bbl/h).

Conclusion

This paper presents modeling results from a benchmark that highlights key thermomechanical behaviors of the salt cavern during cyclic loading. Hydrogen temperature peaks at approximately 60°C (140 °F) during injections, driving synchronized pressure fluctuations, while the brine temperature increases very slowly. Deviatoric stresses are concentrated near the cavern walls and increase slightly with cumulative loading, indicating potential risk of mechanical instability. The factor of safety evaluates the surrounding salt dilatancy to prevent microcracking, while the Bérest effective stress criterion protects against hydraulic fracturing. The IGtH-IUB results outline some safety requirements for hydrogen operations in a generic salt cavern. A concept for determining the maximum and minimum cavern pressures, as well as for recommending operating rates, was illustrated in a practical example.

Although the approaches to dimensioning hydrogen-filled caverns differ, both teams share a common overarching goal: the robust, safe, and gas-tight operation of salt caverns over an extended operating period. Despite different approaches, it has been shown that there are many similarities in the understanding of safety in salt caverns. For example, the IGtH-IUB degree of utilization approach can be compared very well with the Factor of Safety (*FoS*) concept used by Ineris. The extent of the area around the generic cavern, in which stress in the dilatant area is to be expected, has been calculated in a comparable order of magnitude.

The approaches under maximum internal cavern pressure conditions are also comparable. Both the consideration of the Bérest effective stress at Ineris and the evaluation of the formation of safety zones by the IGtH-IUB lead to similar results regarding the maximum internal cavern pressure.

Both authors also use thermodynamic calculations in their considerations. There are certainly deviations in the results here, but these are explainable and do not lead to completely different results. While Ineris uses the factor of safety for dilatancy evaluation, IGtH-IUB evaluates the infiltration fracture lengths.

Both approaches are helpful in the design and operational phase of hydrogen storage systems. Although each modeling team is responsible for its own results, the results of this work will serve as a starting point for intensive cooperation between France and Germany, allowing them to learn from each other and set new standards for rock mechanical designs of salt caverns. This can, of course, also be applied today to natural gas storage caverns in salt domes and bedded salt formations.

Acknowledgements

This research was partly supported by funding from the Clean Hydrogen Partnership of the EU through the HyPSTER (No. 101006751) and FrHyGe (No. 101137892) projects.

References

Bérest, P., Bergues, J., & Brouard, B. (1999). Review of static and dynamic compressibility issues relating to deep underground caverns. *International Journal of Rock Mechanics and Mining Sciences, 36*(8), 1031–1049.

Brouard, B., & Bérest, P. (2022). Calibration of rock-salt thermal and mechanical parameters based on available field data. In *Proceedings of the SMRI Spring Technical Conference*, Rapid City, SD.

Brouard, B., Bérest, P., & Zakharov, V. (2021). Assessment of cavern stability: Cavern clusters vs. single cavern. In *Proceedings of the SMRI Spring Technical Conference* (Virtual).

Brouard, B., Zakharov, V., & Frangi, A. (2022). Numerical modeling of the complex behaviour of a salt cavern. In *Proceedings of the International Geomechanics Symposium*, ARMA-IGS-202-028. https://doi.org/10.56952/igs-2022-028

Chan, K. S., Brodsky, N. S., Fossum, A. F., Bodner, S. R., & Munson, D. E. (1994). Damage-induced non-associated inelastic flow in rock salt. *International Journal of Plasticity, 10*(6), 623–642.

Cyran, K. (2020). Insight into the shape of salt storage caverns. *Archives of Mining Sciences, 65*. https://doi.org/10.24425/ams.2020.133198

DeVries, K. L., Mellegard, K. D., Callahan, G. D., & Goodman, W. M. (2005). Cavern roof stability for natural gas storage in bedded salt (Topical Report RSI-1829, Contract DE-FG26-02NT41651). *U.S. Department of Energy*. https://doi.org/10.2172/850074

Djizanne, H., & Brouard, B. (2025). Numerical analysis of the mechanical stability of salt caverns for underground hydrogen storage under cyclic solicitations. In *Proceedings of ISRM International Symposium EUROCK 2025 – Expanding the Underground Space*, Trondheim, Norway, 16–20 June. ISBN 978-82-8208-079-8.

Djizanne, H., Brouard, B., & Hévin, G. (2023). Mechanical stability of a salt cavern used for hydrogen storage. In *Proceedings of the 15th ISRM Congress & 72nd Geomechanics Colloquium*, Salzburg, Austria, 2752–2757.

Djizanne, H., Brouard, B., Hévin, G., & Lekoko, C. (2023). Stabilité mécanique à long terme des cavités salines de stockage d'hydrogène. *Revue Française de Géotechnique, 177*(3). https://doi.org/10.1051/geotech/2024023

Djizanne, H., Prats, F., Murillo, C., Pique, S., & Hévin, G. (2024). Risk assessment for hydrogen storage in salt caverns. In *Proceedings of SMRI Fall Technical Conference*, Edmonton, AB, Canada.

Djizanne, H., Zapf, D., Habbani, H., Körner, F., & Brouard, B. (2025). Advanced constitutive models for dimensioning salt caverns in underground hydrogen storage. In *Proceedings of the Mechanical Behavior of Salt XI (SaltMech XI)*, 935–946. ISBN 978-1-032-28220-6.

Hasselkus, F., & Reitze, A. (2022). First successful surveys in hydrogen. In *Proceedings of SMRI Spring Technical Conference*, Rapid City, SD, USA.

Karimi-Jafari, M. (2007). Sur le comportement transitoire des cavités salines profondes (Doctoral dissertation). École Polytechnique, Palaiseau, France.

Lüdeling, C., Spiers, C., Urai, J., & Zapf, D. (2024). Creep of rock salt at low deviatoric stress. *SMRI Research Report: RR2023-3*. In *Proceedings of SMRI Spring Technical Conference*, Krakow, Poland.

Minas, S. (2019). Thermodynamic simulation of salt cavern behavior for gas inventory verification. In *Proceedings of SMRI Fall Technical Conference*, Berlin, Germany.

Nieland, J. D. (2008). Salt cavern thermodynamics – Comparison between hydrogen, natural gas, and air storage. In *Proceedings of SMRI Fall Technical Conference*, Marble Falls, TX, USA.

Reedlunn, B., Kitajima, H., Azzam, A. M. J., Iqbal, O., Jeon, I. K., Chester, F. M., Kim, Y.-R., Chang, K. W., Choens, C., & Ross, T. (2025). Damage-free cyclic loading of rock salt: Experiments and constitutive modeling. In *Proceedings of Mechanical Behavior of Salt XI (SaltMech XI)*, 13–23. ISBN 978-1-032-28220-6.

Rokahr, R. B., & Staudtmeister, K. (1993). Rock mechanical study of the load-bearing behavior of a gas cavern in rock salt after a blowout. In *Proceedings of the 7th International Symposium on Salt*, Kyoto, Japan, Vol. 1, 477–482. Amsterdam: Elsevier. ISBN 0-444-89143-9.

Rokahr, R. B., Staudtmeister, K., Zander-Schiebenhöfer, D. (1997). Development of a New Criterion for the Determination of the Maximum Permissible Internal Pressure for Gas Storage Caverns in Rock Salt. *SMRI Resrearch and Development Project Report, Hannover, 1997*.

Schlichtenmayer, M., & Bannach, A. (2015). Renewable energy storage in salt caverns – A comparison of thermodynamics and permeability between natural gas, air, and hydrogen. *SMRI Research Report RR2015-01*.

Staudtmeister, K., Zapf, D., & Leuger, B. (2011). The influence of different loading scenarios on the thermo-mechanical behavior of a gas storage cavern. In *Proceedings of SMRI Spring Technical Conference*, Galveston, TX, USA.

Voegeli, J. L., Caparroz, S., Mills, B., & Costley, J. (2024). Maximizing salt cavern opportunities in Alberta: The Marguerite Lake CAES and Hydrogen Project. In *Proceedings of SMRI Fall Technical Conference*, Edmonton, AB, Canada.

Voegeli, S. J. (2021). Accuracy of temperature logging for calculating gas inventories in storage caverns. In *Proceedings of SMRI Spring Technical Conference* (Virtual).

Wang, T., Yang, C., Yan, X., Li, Y., Liu, W., Liang, C., & Li, J. (2014). Dynamic response of underground gas storage caverns under seismic loads. *Tunneling and Underground Space Technology, 43*.

Wierczeyko, E. (1972). Determination of cavity forms and volumes spread with Echo-Log. In *Proceedings of SMRI Spring Technical Conference*.

Yıldırım, S., Zapf, D., Staudtmeister, K. (2016): The Lubby-CF constitutive model for the thermo-mechanical behavior of rock salt*, Proceeding of the 4th Itasca Symposium on Applied Numerical Modeling. Itasca. March 7-9, 2016, Lima, Peru*

Yildirim, S. (2018). The Lubby-CF constitutive model for the thermo-mechanical behaviour of rock salt: Current version with recent developments, modifications and extensions. In *Proceedings of the 9th Conference on the Mechanical Behaviour of Salt (SaltMech IX)*, 511–523.

Yildirim, S. (2019). Consideration of the mechanical damage behaviour of salt rock in the calculation of infiltration cracks in the edge area of gas storage caverns (Doctoral dissertation). Leibniz University of Hannover, Germany.

Zapf, D., Rokahr, R. B., Leuger, B., & Yildirim, S. (2019). Influence of infiltration fractures on the stress field in the vicinity of gas storage caverns in rock salt. In *Proceedings of SMRI Spring Technical Conference*, New Orleans, LA, USA.

Zapf, D., Staudtmeister, K., & Rokahr, R. B. (2012). Analysis of thermal-induced fractures in rock salt. In *Proceedings of SMRI Spring Technical Conference*, Regina, Saskatchewan, Canada.

Baumgärtel, L., Körner, F., Leuger, B., & Zapf, D. (2022). Special triaxial experiments on the fracture behavior of hollow rock salt specimens. In *Proceedings of the 56th U.S. Rock Mechanics/Geomechanics Symposium (ARMA 2022)*, Santa Fe, NM.

Bérest, P., Bergues, J., & Brouard, B. (1999). Review of static and dynamic compressibility issues relating to deep underground caverns. *International Journal of Rock Mechanics and Mining Sciences, 36*(8), 1031–1049.

Brouard, B., & Bérest, P. (2022). Calibration of rock-salt thermal and mechanical parameters based on available field data. In *Proceedings of the SMRI Spring Technical Conference*, Rapid City, SD.

Brouard, B., Bérest, P., & Zakharov, V. (2021). Assessment of cavern stability: Cavern clusters vs. single cavern. In *Proceedings of the SMRI Spring Technical Conference* (Virtual).

Brouard, B., Zakharov, V., & Frangi, A. (2022). Numerical modeling of the complex behaviour of a salt cavern. In *Proceedings of the International Geomechanics Symposium*, ARMA-IGS-202-028. https://doi.org/10.56952/igs-2022-028

Chan, K. S., Brodsky, N. S., Fossum, A. F., Bodner, S. R., & Munson, D. E. (1994). Damage-induced non-associated inelastic flow in rock salt. *International Journal of Plasticity, 10*(6), 623–642.

Cyran, K. (2020). Insight into the shape of salt storage caverns. *Archives of Mining Sciences, 65*. https://doi.org/10.24425/ams.2020.133198

DeVries, K. L., Mellegard, K. D., Callahan, G. D., & Goodman, W. M. (2005). Cavern roof stability for natural gas storage in bedded salt (Topical Report RSI-1829, Contract DE-FG26-02NT41651). *U.S. Department of Energy*. https://doi.org/10.2172/850074

Djizanne H. (2014). Mechanical stability of a salt cavern submitted to rapid pressure variations: Application to the underground storage of natural gas, compressed air, and hydrogen (in French). *PhD dissertation*, École Polytechnique, 274p. https://pastel.archives-ouvertes.fr/tel-01130986 (retrieved 5/05/2023).

Djizanne, H., & Brouard, B. (2025). Numerical analysis of the mechanical stability of salt caverns for underground hydrogen storage under cyclic solicitations. In *Proceedings of ISRM International Symposium EUROCK 2025 – Expanding the Underground Space*, Trondheim, Norway, 16–20 June. ISBN 978-82-8208-079-8.

Djizanne, H., Bérest, P. & Brouard, B. (2012). Tensile Effective Stresses in Hydrocarbon Storage Caverns. *In Proceedings of SMRI Fall Meeting*, Bremen, Germany.Baumgärtel, L., Körner, F., Leuger, B., & Zapf, D. (2022). Special triaxial experiments on the fracture behavior of hollow rock salt specimens. In *Proceedings of the 56th U.S. Rock Mechanics/Geomechanics Symposium (ARMA 2022)*, Santa Fe, NM.

Djizanne, H., Brouard, B., & Hévin, G. (2023). Mechanical stability of a salt cavern used for hydrogen storage. In *Proceedings of the 15th ISRM Congress & 72nd Geomechanics Colloquium*, Salzburg, Austria, 2752–2757.

Djizanne, H., Brouard, B., Hévin, G., & Lekoko, C. (2023). Stabilité mécanique à long terme des cavités salines de stockage d'hydrogène. *Revue Française de Géotechnique, 177*(3). https://doi.org/10.1051/geotech/2024023

Djizanne, H., Prats, F., Murillo, C., Pique, S., & Hévin, G. (2024). Risk assessment for hydrogen storage in salt cAssessment for Hydrogen Storage in Salt Caverns. In *Proceedings of SMRI Fall Technical Conference*, Edmonton, AB, Canada.

Djizanne, H., Zapf, D., Habbani, H., Körner, F., & Brouard, B. (2025). Advanced Constitutive Models for Dimensioning Salt Caverns in Underground Hydrogen Storage. In *Proceedings of the Mechanical Behavior of Salt XI (SaltMech XI)*, 935–946. ISBN 978-1-032-28220-6.

Hasselkus, F., & Reitze, A. (2022). First Successful Surveys in Hydrogen. In *Proceedings of SMRI Spring Technical Conference*, Rapid City, SD, USA.

Karimi-Jafari, M. (2007). Sur le comportement transitoire des cavités salines profondes (Doctoral dissertation). École Polytechnique, Palaiseau, France.

Lüdeling, C., Spiers, C., Urai, J., & Zapf, D. (2024). Creep of rock salt at low deviatoric stress. *SMRI Research Report: RR2023-3*. In *Proceedings of SMRI Spring Technical Conference*, Krakow, Poland.

Minas, S. (2019). Thermodynamic simulation of salt cavern behavior for gas inventory verification. In *Proceedings of SMRI Fall Technical Conference*, Berlin, Germany.

Munson D. E. (1997). Constitutive model of creep in rock salt applied to underground room closure, *International Journal of Rock Mechanics and Mining Sciences*, Vol. 34 (2), pp. 233-247, https://doi.org/10.1016/S0148-9062(96)00047-2.

Munson D. E. and Dawson P. R. (1984), Salt constitutive modeling using mechanism maps. *In H. Reginald Hardy, Jr & Michael Langer (eds.)*, Proc. 1st Conf. Mech. Beh. of Salt: 717-737. Clausthal-Zellerfeld: Trans Tech Pub.

Munson, D. E., DeVries, K. L., Fossum, A. F., & Callahan, G. D. (1993). Extension of the M-D model for treating stress drops in salt, *Proc. Mechanical Behavior of Salt III, Palaiseau, France. Ghoreychi, Bérest,*

Hardy et Langer (eds.), Trans Tech Pub, Clausthal-Zellerfeld, Germany, ISBN 0-87849-071-X, 31-44. DOI:10.2172/10173279.

Nieland, J. D. (2008). Salt cavern thermodynamics – Comparison between hydrogen, natural gas, and air storage. In *Proceedings of SMRI Fall Technical Conference*, Marble Falls, TX, USA.

Reedlunn, B., Kitajima, H., Azzam, A. M. J., Iqbal, O., Jeon, I. K., Chester, F. M., Kim, Y.-R., Chang, K. W., Choens, C., & Ross, T. (2025). Damage-free cyclic loading of rock salt: Experiments and constitutive modeling. In *Proceedings of Mechanical Behavior of Salt XI (SaltMech XI)*, 13–23. ISBN 978-1-032-28220-6.

Rokahr, R. B., & Staudtmeister, K. (1993). Rock mechanical study of the load-bearing behavior of a gas cavern in rock salt after a blowout. In *Proceedings of the 7th International Symposium on Salt*, Kyoto, Japan, Vol. 1, 477–482. Amsterdam: Elsevier. ISBN 0-444-89143-9.

Rokahr, R. B., Staudtmeister, K., Zander-Schiebenhöfer, D. (1997). Development of a New Criterion for the Determination of the Maximum Permissible Internal Pressure for Gas Storage Caverns in Rock Salt. *SMRI Research and Development Project Report, Hannover, 1997*.

Schlichtenmayer, M., & Bannach, A. (2015). Renewable energy storage in salt caverns – A comparison of thermodynamics and permeability between natural gas, air, and hydrogen. *SMRI Research Report RR2015-01*.

Staudtmeister, K., Zapf, D., & Leuger, B. (2011). The Influence of Different Loading Scenarios on the Thermo-Mechanical Behavior of a Gas Storage Cavern. In *Proceedings of SMRI Spring Technical Conference*, Galveston, TX, USA.

Voegeli, J. L., Caparroz, S., Mills, B., & Costley, J. (2024). Maximizing salt cavern opportunities in Alberta: The Marguerite Lake CAES and Hydrogen Project. In *Proceedings of SMRI Fall Technical Conference*, Edmonton, AB, Canada.

Voegeli, S. J. (2021). Accuracy of Temperature Logging for Calculating Gas Inventories in Storage Caverns. In *Proceedings of SMRI Spring Technical Conference* (Virtual).

Wang, T., Yang, C., Yan, X., Li, Y., Liu, W., Liang, C., & Li, J. (2014). Dynamic response of underground gas storage caverns under seismic loads. *Tunneling and Underground Space Technology, 43*.

Wierczeyko, E. (1972). Determination of cavity forms and volumes spread with Echo-Log. In *Proceedings of SMRI Spring Technical Conference*.

Yildirim, S. (2018). The Lubby-CF constitutive model for the thermo-mechanical behaviour of rock salt: Current version with recent developments, modifications and extensions. In *Proceedings of the 9th Conference on the Mechanical Behaviour of Salt (SaltMech IX)*, 511–523.

Yildirim, S. (2019). Consideration of the mechanical damage behaviour of salt rock in the calculation of infiltration cracks in the edge area of gas storage caverns (Doctoral dissertation). Leibniz University of Hannover, Germany.

Yıldırım, S., Zapf, D., Staudtmeister, K. (2016): The Lubby-CF constitutive model for the thermo-mechanical behavior of rock salt*. In Proceedings of the 4th Itasca Symposium on Applied Numerical Modeling. Itasca. March 7-9, 2016, Lima, Peru*

Zapf, D. (2014). Dimensioning of gas storage caverns in the salt dome margin area (in German*). PhD dissertation*, Faculty of Civil Engineering and Geodesy of the Gottfried Wilhelm Leibniz University Hannover, 151 p. https://repo.uni-hannover.de/bitstreams/aca9e2eb-c0bf-44c4-993e-f6687eb87b55/download

Zapf, D., Rokahr, R. B., Leuger, B., & Yildirim, S. (2019). Influence of infiltration fractures on the stress field in the vicinity of gas storage caverns in rock salt. In *Proceedings of SMRI Spring Technical Conference*, New Orleans, LA, USA.

Zapf, D., Staudtmeister, K., & Rokahr, R. B. (2012). Analysis of thermal-induced fractures in rock salt. In *Proceedings of SMRI Spring Technical Conference*, Regina, Saskatchewan, Canada